Fluid Model of a Hollow Cathode Discharge

IEPC-2019-874

Presented at the 36th International Electric Propulsion Conference
University of Vienna, Austria
September 15-20, 2019

Xin Chen * and J. Navarro-Cavallé † and E. Ahedo ‡
Equipo de Propulsión Espacial y Plasmas, Universidad Carlos III de Madrid
Av. de la Universidad 30, 28911, Leganés, Madrid, Spain

Abstract: A quasi-neutral, steady-state, one-dimensional axial fluid model for the hollow cathode insert region is presented in this work. As a consequence of variable separation and decoupling, wall reactions appear together with collisions as source or sink terms in the fluid equations. Local balances and global conservations of particle, momentum, and energy are discussed. Two operational regimes are identified, named the LIO (Low Ionization) and the HIO (High Ionization) regimes. In the HIO regime, intense ionization draws neutral density maximum towards the inlet. Further downstream, neutral density drops sharply and it is followed by a region with ion wall loss more than ionization. The occurrence of such a region distinguishes the HIO regime from the LIO regime. Regardless of the regimes, plasma density and ionization degree increase with discharge voltage. Nevertheless, electron temperature drops in the LIO regime and increase in the HIO regime. In the HIO regime, more discharge voltage results in ions to be more backward directed by collisional forces and the electron pressure at the anode sheath edge drops with respect to that at the inlet sheath edge. For enhanced thermionic emission from the insert, the cathode tends to work more in the HIO regime.

*Juan de la Cierva Research Fellow, Bioingeniería e Ingeniería Aeroespacial, xin.chen@uc3m.es.
†Assistant Professor, Bioingeniería e Ingeniería Aeroespacial, jaume.navarro@uc3m.es.
‡Professor, Bioingeniería e Ingeniería Aeroespacial, eduardo.ahedo@uc3m.es .

Nomenclature

n = particle density
u = velocity
T = scalar temperature
p = pressure
I = current
q = heat flux
h = enthalpy flux
ϕ = electric potential
z = axial spatial coordinate
m = mass
$\dot{m}$ = mass flow rate
S = particle production rate due to collisions and wall reactions, $\mathrm{m}^{-3}\,\mathrm{s}^{-1}$
R = momentum production rate (or force density) due to collisions and wall reactions, $\mathrm{N}\,\mathrm{m}^{-3}$
E = energy production rate due to collisions and wall reactions, $\mathrm{J}\,\mathrm{m}^{-3}\,\mathrm{s}^{-1}$
F = combination of above production rates after the substitution of continuity and/or momentum equations
$\hat{\xi}$ = independent variable as a result of the change of variable
$\hat{I}$ = normalized particle flux (or current)
$\hat{M}$ = normalized global momentum balance term
$\hat{Q}$ = normalized global energy balance term
$\mathcal{K}$ = thermal conductivity
ν = collisional frequency in s^{-1}
ε = energy
α_{io} = ionization degree, n/n_n

Subscripts

e = electron
i = ion
n = neutral
s = thermionic electron (at insert wall sheath edge)
p = plasma electron (at insert wall sheath edge), or pressure-related term in the local and global balance
D = the term related to the directed motion only in the local and global balance
h = the term related to enthalpy in the local and global balance
q = the term related to heat flux in the local and global balance
S = insert wall surface
W = insert wall sheath edge
J = inlet back plate
I = inlet sheath edge
A = anode plate
B = anode sheath edge
R = axial-radial coupling term
io = ionization
sw = thermionic electron insert wall reaction
pw = plasma electron insert wall reaction
iw = ion wall reaction
nw = neutral wall reaction
0 = reference value for normalization

I. Introduction

At the beginning of 70s, together with the development of electron-bombardment ion thrusters, the Hollow Cathode (HC) first appeared in electric propulsion devices with the cesium autocathode by Speiser and Bransonm, followed by a smaller neutralizer version by Ernstene et al.[1] Nowadays, HCs are widely used in Hall and ion thrusters as neutralizers and electron bombardment sources.[1–4] HC technologies are also crucial to complete the current loop between electrodynamic tethers and plasma ambient in space.[5] They can also be applied as a spacecraft charging mitigation that modifies the spacecraft potential.[6,7] Due to its broad applications and pivotal roles, the physics of the HC needs to be studied and the important mechanisms beneath operations demands to be understood, as a prerequisite to design efficient and durable HCs.

Traditional zero-dimensional (0D) models study the global current and energy balance of a HC device.[8–10] Due to their simplicity, these models can be used to provide preliminary estimations for cathode designs.[11] Nevertheless, the disadvantages of 0D models can be identified, such as difficulties in calculating emission length and incapabilities to provide spatial variation of plasma properties.[12] To incorporate multiple physical processes, time-dependent 2D models have been developed based on finite-volume technique.[13,14] These powerful models can be directly used to study complicated phenomena and address practical problems such as electrode erosion,[15,16] neutral gas viscosity,[17] and ion acoustic turbulence,[18] et cetera. However, the associated complexity and computational cost lead to difficulties in carrying out parametric analysis that reveals the relevance of physical processes, in isolating causes and effects, in discussing causalities, and thus in providing profound insights. Time-independent 1D model would serve as a balance between simplification and computational cost. Nonetheless, few references can be identified in the past[19,20] and certain level of difficulties in reproducibility is encountered. For this reason, the authors present in this work an 1D axial model. Taking advantage of the relative simplicities in the 1D model, intricate causes of physical phenomena can be better isolated, identified, demonstrated, and discussed from the results. The computational power of modern computers can directly bring about abundant insights of plasma processes to be revealed.

This model was first developed in a recent work[21] based on the variable-separation technique to decouple the axial and radial equations from the general 2D fluid equations. With local wall-reaction frequencies as main coupling parameters, an approximate 2D model can be developed by solving together the two sets of ordinary differential differential equations. Such a method has been successfully applied to Hall thrusters[22] and Helicon thrusters.[23] However, it is important to study the decoupled models separately before incorporating the complete equations.[24] Since the variable-separation method and the procedure to apply cross-sectional average on 2D equation were extensively described in,[21] in this work, the 1D axial model is summarised directly in Sec. 2. Plasma response is analysed in Sec. 3 based on spatial profiles of plasma properties, together with local and global balances of particle, momentum, and energy. Parametric study is carried out in Sec. 4 to analyse the effect of electric power and thermionic emission on plasma response and the balances. Conclusions and discussions are presented in Sec. 5.

II. Model formulation

The orifice-less hollow cathode (HC) considered here is a hollow cylinder of radius R and length L (see Fig. 1 for the half-cross-section schematic). The 1D axial fluid model is developed to solve for the time-independent problem ($\partial/\partial t \approx 0$) of the quasi-neutral plasma ($n = n_e \approx n_i$). The cathode insert (S) is negatively biased relative to the anode plate (A) by an external power supply. Such a circuit can drive a net electron current from the insert to the anode, through the plasma in the cylindrical channel. The dash-dot line is the axial centreline of the cylinder. The dashed lines correspond to sheath edges and enclose the simulated quasi-neutral domain. In this article, to be distinguished with sheath - inside which there is a much stronger electric field - the word plasma will be exclusively used to denote the quasi-neutral simulation domain. The inlet sheath (JI), the insert-wall sheath (SW), and the anode sheath (AB) are considered of negligible width. The back plate J is considered as a dielectric plate and the anode A is a metallic plate at the downstream exit. Neutrals (n) are injected from the back plate. There are losses of plasma ions (i)

and bulk plasma electrons (p) at all boundaries. At the insert wall, thermionic electrons (s) are injected and neutrals also return after ion-wall recombination. In the quasi-neutral plasma, three species are considered, being ions (i), electrons (e), and neutrals (n).

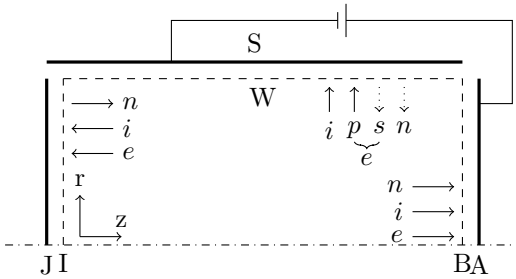

Figure 1: Schematic of a hollow cathode. The dash-dot line corresponds to the centreline of the cathode, with the dashed lines for sheath edges. The symbols p and s stands for plasma and insert electrons, respectively.

A. Assumptions

This model looks for the spatial variation along z of the following plasma properties: plasma potential at the centreline $\phi(z)$; three scalar field properties that are averaged over the circular cross section, being plasma density $n(z)$, neutral density $n_n(z)$, isotropic electron temperature $T_e(z)$; the axial components of four vector field properties, being velocities in directed motion $u_\alpha(z)$ ($\alpha = e, i, n$) and electron heat flux $q_e(z)$. Without taking into account viscosity, electron pressure tensor is thus reduced to isotropic thermodynamic scalar pressure, i.e., $p_e = nT_e$ (T_e with energy units, say Joules). Ion and neutral temperatures are considered to be negligible as $T_e \gg T_n \approx T_i \approx 0$. The reference for electric potential ($\phi = 0$) will be chosen at the insert surface S (an equipotential "grounded" cathode). Particle and momentum conservations are considered for each species . As the main power consumption, energy equation is only solved for electrons, with heat flux approximated by Fourier's law. The time-independent 1D axial equations in the conservative form are

$$\frac{\mathrm{d}\left(nu_e\right)}{\mathrm{d}z} = S_e \ , \tag{1a}$$

$$\frac{\mathrm{d}\left(nu_i\right)}{\mathrm{d}z} = S_i \ , \tag{1b}$$

$$\frac{\mathrm{d}\left(nu_n\right)}{\mathrm{d}z} = S_n \ , \tag{1c}$$

$$\frac{\mathrm{d}\left(m_e n u_e^2\right)}{\mathrm{d}z} + \frac{\mathrm{d}p_e}{\mathrm{d}z} = R_e + en_e\frac{\mathrm{d}\phi}{\mathrm{d}z} \ , \tag{1d}$$

$$\frac{\mathrm{d}\left(m_i n u_i^2\right)}{\mathrm{d}z} = R_i - en_e\frac{\mathrm{d}\phi}{\mathrm{d}z} \ , \tag{1e}$$

$$\frac{\mathrm{d}\left(m_i n_n u_n^2\right)}{\mathrm{d}z} = R_n \ , \tag{1f}$$

$$\frac{\mathrm{d}\left[\left(\dfrac{m_e n u_e^2}{2} + \dfrac{5}{2}p_e\right)u_e + q_e\right]}{\mathrm{d}z} = E_e + enu_e\frac{\mathrm{d}\phi}{\mathrm{d}z} \ , \tag{1g}$$

$$q_e = -\mathcal{K}_e\frac{\mathrm{d}T_e}{\mathrm{d}z} \ . \tag{1h}$$

As a result of variable-separation and decoupling, the particle, momentum, and energy fluxes at the insert wall become sources (or sinks) of particle, momentum, and energy. The effects of collisions and wall reactions on each species are included in S_α as *particle production rate* in $\mathrm{m^{-3}\,s^{-1}}$, R_α as *momentum production rate*

or *force density* in $\mathrm{N\,m^{-3}}$, and E_e as *energy production rate* in $\mathrm{J\,m^{-3}\,s^{-1}}$:

$$S_e = S_{e,io} + S_{e,sw} + S_{e,pw} \ , \tag{2a}$$
$$S_i = S_{i,io} + S_{i,iw} \ , \tag{2b}$$
$$S_n = S_{n,io} + S_{n,iw} \ , \tag{2c}$$
$$R_e = R_{e,ei} + R_{e,en} + R_{e,pw} \ , \tag{2d}$$
$$R_i = R_{i,ei} + R_{i,in} + R_{i,io} + R_{i,iw} \ , \tag{2e}$$
$$R_n = R_{n,en} + R_{n,in} + R_{n,io} \ , \tag{2f}$$
$$E_e = E_{e,io} + E_{e,ei} + E_{e,en} + E_{e,sw} + E_{e,pw} \ . \tag{2g}$$

The subscript after comma denotes the type of collision or wall reaction. The collisions considered in this model are:

- Ionization (subscript *io*) is a source of particles for electrons and ions with $S_{e,io} = S_{i,io} = n\nu_{io}$ (ν stands for collisional frequency), yet a sink of neutral particles with $S_{n,io} = -S_{i,io}$. If ionization creates ions with the velocity of neutrals, it then appears in ion momentum equation as a source of momentum with $R_{i,io} = m_i n \nu_{io} u_n$, with the opposite for neutrals $R_{n,io} = -R_{i,io}$. Ionization mainly consumes electron energy as $E_{e,io} = -n\nu_{io}\varepsilon_{io}$, with ε_{io} for the first ionization energy.
- The *e*-*i* elastic Coulomb collision (subscript *ei*) and *e*-*n* elastic collision (subscript *en*) can be expressed as frictional forces on electrons as $R_{e,ei} = -m_e n \nu_{ei}(u_e - u_i)$ and $R_{e,en} = -m_e n \nu_{en}(u_e - u_n)$, with the opposite for ions and neutrals as $R_{i,ei} = -R_{e,ei}$ and $R_{n,en} = -R_{e,en}$. The random motion energy exchange due to these two collisions consumes electron energy with $E_{e,ei} + E_{e,en} = -\dfrac{3m_e}{m_i} n \left(\nu_{ei} + \nu_{en}\right) T_e$. Both collisions determine the thermal conductivity in Fourier heat conduction equation as $\mathcal{K}_e \approx \dfrac{5}{2} \dfrac{nT_e}{m_e \left(\nu_{en} + \nu_{ei}\right)}$.
- The *i*-*n* CEX collision (subscript *in*) can be written as a frictional force on ions as $R_{i,in} = -\dfrac{1}{2} m_i n \nu_{in} (u_i - u_n)$, with the opposite for neutrals as $R_{n,in} = -R_{i,in}$.

The models used for cross-sectional averaged collisional frequencies were described in.[21] Wall-reaction terms are defined through frequencies for thermionic emission from insert (ν_{sw}), plasma electron absorption (ν_{pw}), and plasma ion recombination (ν_{iw}). Their associated production rates are presented in A. Since wall reactions are treated mathematically as collisions in the 1D model, "collisional terms" can be used to include both collisions and wall reactions hereafter.

B. Normalization and isolation of variables

The reference quantities for normalization are

$$g_0 \equiv \frac{\dot{m}}{\pi R^2 m_i}, \quad u_0 \equiv \sqrt{\frac{T_0}{m_i}}, \quad z_o \equiv R \ ,$$
$$n_0 \equiv \frac{g_0}{u_0}, \quad q_0 \equiv T_0 g_0 \ ,$$

with T_0 as an arbitrary parameter to normalize energies and $\dot{m}$ the given mass flow rate. The system of equations are normalized using the reference quantities for the production rates,

$$S_0 \equiv \frac{g_0}{z_0}, \quad R_0 \equiv \frac{T_0 n_0}{z_0}, \quad E_0 \equiv \frac{T_0 g_0}{z_0} \ .$$

After linear recombinations, the isolated derivatives become

$$\frac{\mathrm{d}\hat{z}}{\mathrm{d}\hat{\xi}} = \left(\hat{T}_e - \hat{u}_i^2 - \hat{m}_e\hat{u}_e^2\right) \ , \tag{3a}$$

$$\frac{\mathrm{d}\left(\ln\hat{n}\right)}{\mathrm{d}\hat{\xi}} = \hat{F}_3 + \hat{F}_4 - \hat{F}_7 - \hat{F}_2\hat{u}_i - \hat{F}_1\hat{m}_e\hat{u}_e \ , \tag{3b}$$

$$\frac{\mathrm{d}\hat{u}_e}{\mathrm{d}\hat{\xi}} = \hat{F}_1\frac{\mathrm{d}\hat{z}}{\mathrm{d}\hat{\xi}} - \frac{\mathrm{d}\left(\ln\hat{n}\right)}{\mathrm{d}\hat{\xi}}\hat{u}_e \ , \tag{3c}$$

$$\frac{\mathrm{d}\hat{u}_i}{\mathrm{d}\hat{\xi}} = \hat{F}_2\frac{\mathrm{d}\hat{z}}{\mathrm{d}\hat{\xi}} - \frac{\mathrm{d}\left(\ln\hat{n}\right)}{\mathrm{d}\hat{\xi}}\hat{u}_i \ , \tag{3d}$$

$$\frac{\mathrm{d}\hat{\phi}}{\mathrm{d}\hat{\xi}} = \hat{T}_e\frac{\mathrm{d}\left(\ln\hat{n}\right)}{\mathrm{d}\hat{\xi}} + \hat{m}_e\hat{u}_e\frac{\mathrm{d}\hat{u}_e}{\mathrm{d}\hat{\xi}} + \left(\hat{F}_7 - \hat{F}_3\right)\frac{\mathrm{d}\hat{z}}{\mathrm{d}\hat{\xi}} \ , \tag{3e}$$

$$\frac{\mathrm{d}\hat{u}_n}{\mathrm{d}\hat{\xi}} = \frac{\hat{F}_5}{\hat{u}_n}\frac{\mathrm{d}\hat{z}}{\mathrm{d}\hat{\xi}} \ , \tag{3f}$$

$$\frac{\mathrm{d}\hat{q}_e}{\mathrm{d}\hat{\xi}} = \hat{F}_6\frac{\mathrm{d}\hat{z}}{\mathrm{d}\hat{\xi}} - \frac{3}{2}\hat{n}\hat{u}_e\hat{F}_7\frac{\mathrm{d}\hat{z}}{\mathrm{d}\hat{\xi}} + \hat{n}\hat{u}_e\hat{T}_e\frac{\mathrm{d}\left(\ln\hat{n}\right)}{\mathrm{d}\hat{\xi}} \ , \tag{3g}$$

$$\frac{\mathrm{d}\hat{T}_e}{\mathrm{d}\hat{\xi}} = \hat{F}_7\frac{\mathrm{d}\hat{z}}{\mathrm{d}\hat{\xi}} \ , \tag{3h}$$

$$\hat{n}_n = \frac{1 - \hat{n}\hat{u}_i}{\hat{u}_n} \ , \tag{3i}$$

with the electron-to-ion mass ratio $\hat{m}_e = m_e/m_i$ and the upper hat symbol for dimensionless quantity.

The change of variable (from $\hat{z}$ to $\hat{\xi}$) was applied to regulate the problem, thus avoiding the numerical difficulties by cause of the sonic condition $\hat{T}_e - \hat{u}_i^2 - \hat{m}_e\hat{u}_e^2 = 0$. This sonic condition is *singular* if the right-hand side (RHS) of Eq. (3b) is *not zero*, thus $\mathrm{d}(\ln\hat{n})/\,\mathrm{d}\hat{\xi} \neq 0$ and $\mathrm{d}(\ln\hat{n})/\,\mathrm{d}\hat{z} \to \infty$. This type of sonic condition is permitted at the boundaries, where quasi-neutrality breaks down and matching to a non-neutral sheath solution is required. In this case, the ion sonic velocity $\hat{c}_s = \sqrt{\hat{T}_e - \hat{m}_e\hat{u}_e^2}$ corresponds to the minimum ion speed required by the general Bohm sheath criteria $\hat{u}_i \geq \hat{c}_s$. However, inside the quasi-neutral plasma, a *regular* sonic point can arise if the RHS of Eq. (3b) is *zero*, thus $\mathrm{d}(\ln\hat{n})/\,\mathrm{d}\hat{\xi} = 0$. Consequently, all derivatives to $\hat{\xi}$ would vanish at that point, yet without singularities due to finite derivatives to $\hat{z}$. In this work, the latter case is not considered. Ions are thus subsonic in the plasma and singular conditions occur at the sheath edges.

The F-terms contain all collisions. Electron and ion particle production rates in continuity equations directly give rise to particle production frequencies F_1 and F_2 as

$$nF_{1,2} = S_{e,i} \ . \tag{4}$$

In the momentum equations, substituting the advective term $mu\,\mathrm{d}(nu)/\,\mathrm{d}z$ with continuity equations leads to

$$nF_{3,4} = R_{e,i} - m_{e,i}u_{e,i}S_{e,i}, \ \ n_nF_5 = R_n - m_nu_nS_n \ . \tag{5}$$

In the electron energy equation, the substitution of continuity and momentum equations lead to

$$F_6 = E_e - u_eR_e + \left(\frac{m_eu_e^2}{2} - \frac{5}{2}T_e\right)S_e \ . \tag{6}$$

Thermal conductivity is included in the term F_7 (equal to temperature gradient). For the purpose of reproducibility, the mathematical equations of these terms in dimensionless form are listed in B.

In the axial problem, there are eight ODEs and one algebraic equation. They will be solved together with the boundary conditions (BCs) to find the spatial profiles of the following nine variables: $\hat{z},\ \ln\hat{n},\ \hat{n}_n,\ \hat{u}_e,\ \hat{u}_i,\ \hat{u}_n,\ \hat{\phi},\ \hat{q}_e,\ \hat{T}_e$.

C. Boundary conditions

1. *Inlet sheath edge* ***I***

At the inlet sheath edge I, the floating condition $\hat{n}(\hat{u}_i - \hat{u}_e) = 0$ and the singular sonic condition are applied as

$$\hat{u}_{e,I} = \hat{u}_{i,I} = -\sqrt{\hat{T}_{e,I}/\left(1+\hat{m}_e\right)} \ . \tag{7}$$

Due to a negligible directed motion compared with random thermal motion, electrons can be considered as near-Maxwellian at I. Only electrons with sufficiently high energy can overcome sheath potential barrier, thus escaping plasma. Therefore, the inlet sheath drop $\hat{\phi}_{JI} = \hat{\phi}_I - \hat{\phi}_J$ determines the electron flux,[25] giving the relation

$$\hat{\phi}_{JI} = -\hat{T}_{e,I} \ln\left(|\alpha_{ue,I}|\right) > 0 \ , \tag{8}$$

with $\alpha_{ue} = \hat{u}_e/\sqrt{\hat{T}_e/(2\pi\hat{m}_e)}$. The assumption of an electron-repelling sheath ($\hat{\phi}_{JI} > 0$) requires $|\alpha_{ue,I}| < 1$. For this reason, the velocity ratio α_{ue} is intended to inspect the validity of such an assumption. Given by Eq. (7), this condition is certainly satisfied at the inlet. The total electron energy flux at I is also determined by these high-energy Maxwellian electrons as[25]

$$\hat{Q}_{e,I} = \hat{n}_I \hat{u}_{e,I} \left(\hat{\phi}_{JI} + 2\hat{T}_{e,I}\right) < 0 \ . \tag{9}$$

Considering negligible the kinetic energy flux in directed motion, heat flux is thus obtained by excluding the enthalpy flux $5\hat{n}_I\hat{u}_{e,I}\hat{T}_{e,I}/2$,

$$\hat{q}_{e,I} = \hat{n}_I \hat{u}_{e,I} \left(\hat{\phi}_{JI} - \hat{T}_{e,I}/2\right) \ . \tag{10}$$

The system of equations, Eqs. (3), can be forwardly integrated from $\hat{\xi} = \hat{z} = 0$ as an inlet-boundary-condition (IBC) problem. For a chosen value of $\hat{u}_{n,I}$, the sheath models described above can be used to derive all IBCs from $\hat{\phi}_I$, $\hat{n}_I$, and $\hat{T}_{e,I}$. For this reason, these three IBCs are chosen as *shooting unknowns*, which will be found by a *shooting method* to fulfil three *shooting targets* given by the BCs downstream (see below).

2. *Anode sheath edge* ***B***

The anode sheath is also considered to be conventionally electron-repelling ($\hat{\phi}_{AB} = \hat{\phi}_B - \hat{\phi}_A > 0$), with the singular sonic condition fulfilled at the edge as

$$\hat{u}_{i,B} = \sqrt{\hat{T}_{e,B} - \hat{m}_e \hat{u}_{e,B}^2} \ . \tag{11}$$

For the sheath drop, the same model is applied as that at the inlet:

$$\hat{\phi}_{AB} = -\hat{T}_{e,B} \ln\left(\alpha_{ue,B}\right) > 0 \ . \tag{12}$$

Due to large thermionic emission as electron source (after all, electron current needs to be driven for being a cathode), a fast electron fluid can result in $\alpha_{ue,B} > 1$. In this case, the assumption of an electron-repelling anode sheath can be violated and modifications on the model would be required (not included in this work).

If the sonic condition is chosen as the *stop criterion* for the IBC integration problem, the simulation length $\hat{z}_B$ obtained from Eq. (3a) would change for different *shooting unknowns*. Therefore, the cathode tube length becomes a *shooting target* (denoted by the asterisk superscript) as

$$\hat{z}_B^* = L/z_0 \ . \tag{13}$$

The second *shooting target* arises from the discharge voltage (anode-to-insert voltage V_d) set by power source,

$$\hat{\phi}_A^* = eV_d/T_0 \ . \tag{14}$$

This needs to match $\phi_A = \phi_B - \phi_{AB}$, with ϕ_B from integrating Eq. (3e) and ϕ_{AB} from the sheath model Eq. (12). The last *shooting target* is given by the heat flux permitted by the sheath potential drop

$$\hat{q}_{e,B}^* = \hat{n}_B \hat{u}_{e,B} \left(\hat{\phi}_{AB} - \hat{T}_{e,B}/2 \right) \ , \tag{15}$$

which must agree with $\hat{q}_{e,B}$ obtained from Eq. (3g).

D. The complete mathematical problem

In conclusion, the system of ODEs can be first integrated as an IBC problem using Runge-Kutta method. Then, as a *shooting problem* that looks for proper IBCs fulfilling the *shooting targets* at B, the following implicit equations

$$\begin{gathered} \boldsymbol{f}(\boldsymbol{x}) = 0 \ , \quad \boldsymbol{x} = [\hat{T}_{e,I}; \quad \hat{n}_I, \quad \hat{\phi}_I] \ , \\ \boldsymbol{f} = [f_z = \hat{z}_B - \hat{z}_B^*; \ \ f_q = \hat{q}_{e,B} - \hat{q}_{e,B}^*; \ \ f_\phi = \hat{\phi}_A - \hat{\phi}_A^*] \end{gathered} \tag{16}$$

need to be solved by an iterative scheme. In this way, for a given gas type, the steady plasma response (axial profiles of the *variables*) is found for the following set of dimensionless *parameters*,

$$\hat{T}_s, \quad \hat{S}_{ew,s}, \quad \hat{u}_{n,I}, \quad \hat{z}_B, \quad \hat{\phi}_A \ . \tag{17}$$

Since the discharge voltage V_d is chosen as a constraint, the discharge (electron) current I_d thus becomes an *output* from the simulation, instead of being a *parameter*. Inside the sheaths, because ionization is negligible, continuity equation guarantees a constant current as $I_{e,A} = I_{e,B}$ and $I_{i,A} = I_{i,B}$. The normalized discharge current thus becomes

$$I_d = I_0 \hat{I}_d, \quad \hat{I}_d = \hat{I}_{e,B} - \hat{I}_{i,B}, \quad I_0 = e\pi R^2 g_0 \ , \tag{18}$$

with $\hat{I}_{e,i} = \hat{n}\hat{u}_{e,i}$ the normalized particle flux.

To reduce computational cost and improve convergence, the equation f_ϕ and the unknown $\hat{\phi}_I$ are removed from the equation system, left with two unknowns $\boldsymbol{x} = [\hat{T}_{e,I}; \hat{n}_I]$ and two equations $\boldsymbol{f} = [f_z; f_q]$. Then, $\hat{\phi}_I$ becomes a *parameter*, while the discharge voltage $\hat{\phi}_A$ becomes an *output* (as the discharge current $\hat{I}_d$). In this way, by varying $\hat{\phi}_I$, HC current-voltage (IV) characteristic can be reconstructed with less numerical difficulties. Nevertheless, this is not the only advantage. By reducing the number of unknowns from three to two, contour maps (or surfaces) of $\boldsymbol{f}(\boldsymbol{x})$ can be obtained by integrating the IBC problem. Such visualization tools can be straightforwardly used to discuss existence and uniqueness of the solutions for $\boldsymbol{f}(\boldsymbol{x}) = 0$. Moreover, they can be used to obtain good initial guesses, instead of relying on tedious continuation methods.

In this work, the plasma response will first be analysed from the spatial profiles for one set of parameters. The influence of discharge voltage and thermionic emission on plasma response will be examined. Insert material is Lanthanum hexaboride (LaB_6) with $\phi_{wf} = 2.66\,\mathrm{eV}$ and $A_G = 2.9 \times 10^5\,\mathrm{A\,m^{-2}\,K^{-2}}$.[26] The cathode insert has dimensions of $R = 0.5\,\mathrm{mm}$ and $L = 1.5\,\mathrm{mm}$. The gas is Xenon with $\hat{m}_e \approx 4.179 \times 10^{-6}$ and $\varepsilon_{io} = 12.127\,\mathrm{eV}$. Mass flow rate is $3.6\,\mathrm{sccm}$ ($0.354\,\mathrm{mg\,s^{-1}}$). The reference temperature and neutral velocity are chosen to be $T_0 = 4\,\mathrm{eV}$ and $\hat{u}_{n,I} = 0.2$. Results will be shown in dimensionless quantities. To recover important dimensional quantities, some reference values are listed here: $n_0 \approx 1.287 \times 10^{19}\,\mathrm{m^{-3}}$, $u_0 \approx 1.715\,\mathrm{km\,s^{-1}}$, $I_0 \approx 0.278\,\mathrm{A}$.

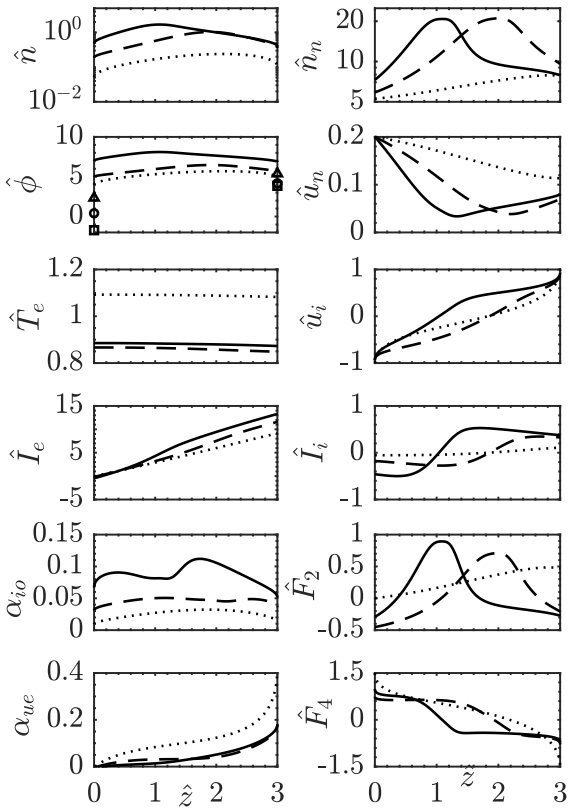

Figure 2: Spatial profiles of plasma parameters for $\hat{\phi}_I = 7$ ($\hat{\phi}_A \approx 5.36$, solid, triangle), $\hat{\phi}_I = 5$ ($\hat{\phi}_A \approx 4.12$, dashed, circle), $\hat{\phi}_I = 4$ ($\hat{\phi}_A \approx 3.91$, dotted, square).

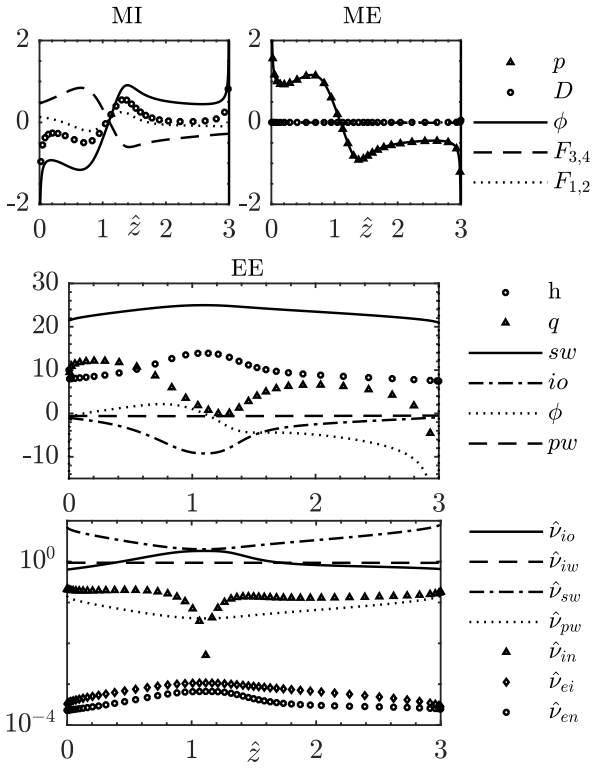

Figure 3: Local momentum balance, local energy balance, and collisional frequencies for $\hat{\phi}_I = 7$. The legends are described in correspondent subsections. The normalization of the dimensionless collisional frequencies are shown in B.

III. Insight of one specific solution

For $T_s = 1650\,\mathrm{K}$ ($\hat{T}_s \approx 0.0356$, $\hat{S}_{e,sw} \approx 3.352$) and $\hat{\phi}_I = 7$ ($\hat{\phi}_A \approx 5.36$), the solution of $\boldsymbol{f}(\boldsymbol{x}) = 0$ is found to be $\hat{n}_I \approx 0.49$ and $\hat{T}_{e,I} \approx 0.89$. Spatial profiles of plasma variables are shown in Fig. 2 by the solid curves. To understand these profiles, it is necessary to analyse the global and local balances of particle, momentum, and energy.

First of all, due to small electron mass and thus high thermal conductivity $\hat{\mathcal{K}}_e \sim 1 \times 10^3$ (consistent with $\hat{\nu}_{ei}, \hat{\nu}_{en} \sim 1 \times 10^{-4}$ in Fig. 3), the temperature gradients are negligible. For this reason, analyses will be carried out without taking into account the temperature variation. However, although constant temperature is an adequate assumption, it is still necessary to include energy equation to fulfil energy conservation. Moreover, it was also found that, without energy equation ($\hat{T}_e$ as a *parameter*), two solutions can normally be found for $f_z(\hat{n}_{z,I}) = 0$. It seems that energy conservation renders one of these two solutions far-away from being correct. Then, the solution for $\boldsymbol{f}(\hat{T}_{e,I}, \hat{n}_I) = 0$ was found to be unique (although rigorous *proof* was not intended).

A. Local plasma momentum balance

To present local electron momentum balance, the ME panel of Fig. 3 plots each term in the dimensionless momentum equation

$$\frac{\mathrm{d}\left(\hat{m}_e \hat{n} \hat{u}_e^2\right)}{\mathrm{d}\hat{z}} + \frac{\mathrm{d}\hat{p}_e}{\mathrm{d}\hat{z}} = \hat{n}\frac{\mathrm{d}\hat{\phi}}{\mathrm{d}\hat{z}} + \hat{n}\hat{F}_3 + \hat{m}_e \hat{u}_e \hat{n}\hat{F}_1 \ . \tag{19}$$

From left to right, these terms are electron inertia (momentum density flux gradient in directed motion, legend D), pressure gradient (or momentum density flux gradient in random motion, legend p), electric force density (legend ϕ), and the collisional terms (legend F_3 and F_1). In this case, electron inertia and collisional terms are negligible due to the small electron mass ($\hat{m}_e \ll 1$). Locally at any z, electron momentum balance is thus a balance between the electron pressure gradient and the electric force density, which leads to the familiar Boltzmann relation $\hat{T}_e\,\mathrm{d}\left(\ln \hat{n}\right)/\,\mathrm{d}\hat{z} \approx \mathrm{d}\hat{\phi}/\,\mathrm{d}\hat{z}$. For this reason, the behaviour of the potential $\hat{\phi}$ is found to follow closely that of the plasma density $\hat{n}$ in Fig. 2.

The dimensionless ion momentum equation reads

$$\frac{\mathrm{d}\left(\hat{n}\hat{u}_i^2\right)}{\mathrm{d}\hat{z}} = -\hat{n}\frac{\mathrm{d}\hat{\phi}}{\mathrm{d}\hat{z}} + \hat{n}\hat{F}_4 + \hat{u}_i \hat{n}\hat{F}_2 \ . \tag{20}$$

As shown in the MI panel of Fig. 3, ion inertia is certainly not negligible. After cancelling out the advective term $\hat{u}_i\,\mathrm{d}(\hat{n}\hat{u}_i)/\,\mathrm{d}\hat{z}$ with $\hat{u}_i\hat{n}\hat{F}_2$, the remaining inertia term $\hat{n}\hat{u}_i\,\mathrm{d}\hat{u}_i/\,\mathrm{d}\hat{z}$ is shown in the graph by the difference between the D-curve and the F_2-curve. By comparing with other curves, this term is again small, with exceptions only near the singularities at boundaries. Therefore, local ion momentum balance becomes a balance between electric field and $\hat{F}_4$, i.e. $\mathrm{d}\hat{\phi}/\,\mathrm{d}\hat{z} \approx \hat{F}_4$. Combining electron and ion momentum equations, the plasma response can be summarised by

$$\hat{T}_e \frac{\mathrm{d}(\ln \hat{n})}{\mathrm{d}\hat{z}} \approx \frac{\mathrm{d}\hat{\phi}}{\mathrm{d}\hat{z}} \approx \hat{F}_4 \approx -\left(\hat{\nu}_{io} + \hat{\nu}_{in}\right)\left(\hat{u}_i - \hat{u}_n\right) \ , \tag{21}$$

with ionization and CEX collision being the dominant collisions. Therefore, electric field becomes a bridge that couples with plasma density through electron response and links to collisions in ion response. Consequently, as shown in Fig. 2, the maxima of plasma density and electric potential thus occur close to $\hat{u}_i = \hat{u}_n$ and $\hat{F}_4 \approx 0$ ($\hat{z} \approx 1.2$). Prior to his location, plasma density increases for $\hat{u}_i < \hat{u}_n$.

B. Neutral particle and momentum balance

Neutral continuity and momentum equations can be written as

$$\frac{\mathrm{d}\hat{u}_n}{\mathrm{d}\hat{z}} + \hat{u}_n \frac{\mathrm{d}(\ln \hat{n}_n)}{\mathrm{d}\hat{z}} = -\alpha_{io}\hat{F}_2 \ , \quad \frac{\mathrm{d}\hat{u}_n}{\mathrm{d}\hat{z}} = \frac{\hat{F}_5}{\hat{u}_n} \ , \tag{22}$$

with $\alpha_{io} = \hat{n}/\hat{n}_n$ the ionization degree. For neutrals, due to $T_n \approx 0$, $\hat{F}_5$ governs the velocity gradient and, then, the density gradient responds according to the continuity equation. Considering dominant collisions, the combination of both equations leads to

$$\frac{\hat{u}_n}{\alpha_{io}} \frac{\mathrm{d}(\ln \hat{n}_n)}{\mathrm{d}\hat{z}} = -\hat{F}_2 - \frac{\hat{F}_5}{\alpha_{io}\hat{u}_n} \approx -\hat{\nu}_{io} - \hat{\nu}_{in}\left(\frac{\hat{u}_i}{\hat{u}_n} - 1\right) \ . \tag{23}$$

Therefore, a positive neutral density gradient (see Fig. 2) can only arise in the case of $\hat{\nu}_{io} < \hat{\nu}_{in}(1 - \hat{u}_i/\hat{u}_n)$, with sufficient CEX collisions and $\hat{u}_n > \hat{u}_i$. The maximum neutral density occurs at $\hat{\nu}_{io} \approx \hat{\nu}_{in}(1-\hat{u}_i/\hat{u}_n)$. Its location (before $\hat{u}_i < 0$) is followed by that of maximum plasma density with $\hat{u}_i \approx \hat{u}_n$ and that of minimum neutral velocity with $\hat{\nu}_{iw} \approx \hat{\nu}_{in}(\hat{u}_i/\hat{u}_n - 1)$. After the maximum, the effect of ionization to consume neutrals and decrease neutral density is well pronounced. After $\hat{u}_i = \hat{u}_n$, a region with sharp neutral density drop is observed owing to both ionization consumption and CEX collision as momentum source. However, since $\hat{\nu}_{io}$ and $\hat{\nu}_{in}$ both decrease with $\hat{n}_n$, this region is followed by another region with a moderate slope.

C. Plasma particle conservation

In a time-independent 1D model,the continuity equation depicts how the particle production rate due to ionization and wall reaction is balanced, *locally*, with the gradient of particle density flux ($\mathrm{d}\hat{I}_{e,i}/\,\mathrm{d}\hat{z} = \hat{n}\hat{F}_{1,2}$). Ionization and ion wall loss would increase and decrease ion flux, respectively. The slope of $\hat{I}_i$ in Fig. 2 thus follows the sign of $\hat{F}_2 = \hat{\nu}_{io} - \hat{\nu}_{iw}$. Electron flux is increased by thermionic emission and ionization, while decreased by plasma electrons leaving to the insert. However, due to $\hat{\nu}_{pw} \ll \hat{\nu}_{sw}$, $\hat{\nu}_{io}$, electron flux increases towards anode.

The volumetric integration of Eqs. (1a) and (1b) leads to the *global* charge conservation, which is a balance between the fluxes leaving at both ends ($\hat{I}_{\alpha,IB} = \hat{I}_{\alpha,B} - \hat{I}_{\alpha,I}$) and the volumetric integration of particle production rates ($\hat{I}_{\alpha,k} = \int_0^{\hat{z}_B} \hat{S}_{\alpha,k}\,\mathrm{d}\hat{z}$ for k-type collision):

$$\hat{I}_{i,IB} = \hat{I}_{i,io} + \hat{I}_{i,iw} \ , \quad \hat{I}_{e,IB} = \hat{I}_{e,io} + \hat{I}_{e,sw} + \hat{I}_{e,pw} \ . \tag{24}$$

Because floating condition is applied at the inlet and ionization produces same amount of electrons and ions $\hat{I}_{i,io} = \hat{I}_{e,io}$, the discharge current in Eq. (18) to anode thus balances insert-wall reactions as

$$\hat{I}_d = \hat{I}_{e,B} - \hat{I}_{i,B} = \hat{I}_{e,sw} + \hat{I}_{e,pw} - \hat{I}_{i,iw} \ . \tag{25}$$

At the insert wall, (electron) discharge current is constituted by sources from thermionic electron and ion wall recombination, plus sinks due to plasma electron loss. If there is abundant thermionic emission and sufficiently large sheath drop to repel back plasma electrons, a net electron current can be secured by $\hat{\nu}_{sw} + \hat{\nu}_{iw} > \hat{\nu}_{pw}$.

D. Global plasma momentum conservation

Similar to particle conservation, *global* momentum conservation for each charged species can be found by the volumetric integral of Eqs. (19) and (20). Summing both gives the global plasma momentum conservation,

$$\hat{M}_{iD,IB} + \hat{M}_{eD,IB} + \hat{M}_{ep,IB} = \hat{M}_{e,R} + \hat{M}_{i,R} \ . \tag{26}$$

On the RHS, it is the global volumetric momentum production rate due to collisions $\hat{M}_{\alpha,R} = \int_0^{\hat{z}_B} \hat{R}_\alpha\,\mathrm{d}\hat{z}$. On the LHS, those are the momentum fluxes leaving the boundaries, including both directed motion, $\hat{M}_{\alpha D,IB} = \hat{m}_\alpha\left(\hat{n}_B\hat{u}^2_{\alpha,B} - \hat{n}_I\hat{u}^2_{\alpha,I}\right)$, and random motion, $\hat{M}_{ep,IB} = \hat{p}_{e,B} - \hat{p}_{e,I}$. Since sonic conditions are applied at both ends, the directed plasma momentum flux outwards is equal to the pressure difference as $\hat{M}_{iD,IB} + \hat{M}_{eD,IB} = \hat{p}_{e,B} - \hat{p}_{e,I}$. Consequently, considering dominant collisions, the global momentum balance can be

approximated by

$$2\left(\hat{p}_{e,B}-\hat{p}_{e,I}\right)\approx\hat{M}_{i,R}$$
$$\approx\int_0^{\hat{z}_B}\hat{n}\left[\hat{\nu}_{io}\hat{u}_n-\hat{\nu}_{iw}\hat{u}_i-\hat{\nu}_{in}\left(\hat{u}_i-\hat{u}_n\right)\right]\mathrm{d}\hat{z}\ . \tag{27}$$

If, globally, collisions introduce to ions more backward momentum than forward momentum, the electron pressure at B needs to drop below the electron pressure at I. In the current case of study, $\hat{p}_{e,B}<\hat{p}_{e,I}$ (see $\hat{n}$ in Fig. 2) signifies that ions are mainly directed backwards by collisions.

E. Plasma velocities

The importance of discussing plasma velocities lies in the fact that plasma needs to self-adjust to fulfil the constraints at the boundaries. Sonic conditions (Bohm criteria) are applied at both ends as boundary conditions on ion velocities. The variation of electric potential is mainly concentrated inside sheaths. Therefore, to satisfy the constraint given by discharge voltage, electron velocity becomes crucial because sheath drop depends on the velocity ratio α_{ue} as in Eq. (12). However, owing to the coupling of fluid equations, it is not a single mechanism that decides the velocities. In this work, the velocity variation is discussed from the aspect of velocity gradient. Apparently, it is more convenient to discuss the velocity gradient through continuity equation in the form of Eqs. (3c) and (3d), as governed by the difference between the density gradients and the particle production terms $\hat{F}_{1,2}$.

For ions, it is found that the density gradient dominates at the boundaries and the magnitude of ion velocity is increased (or ions are accelerated) towards the direction of dropping density. Nevertheless, around the maximum plasma density ($\hat{u}_i\approx\hat{u}_n$ and $\hat{F}_4\approx 0$), it is sufficient ionization ($\hat{F}_2=\hat{\nu}_{io}-\hat{\nu}_{iw}>0$) that guarantees a positive velocity gradient. Since ionization consumes neutrals and thus reduces $\hat{\nu}_{io}$, a sudden reduction of velocity gradient occurs near $\hat{\nu}_{io}=\hat{\nu}_{iw}$ ($\hat{z}\approx 1.7$), beyond which ions tend to lose velocity due to insufficient ionization ($\hat{F}_2<0$). However, owing to dropping density downstream, a positive velocity gradient is sustained.

By the same token, abundant thermionic current from insert ($\hat{\nu}_{sw}$ in $\hat{F}_1$) would also result in a fast electron fluid downstream. As shown in Eq. (12), the assumption of conventional electron-repelling anode sheath sets an upper limit on electron velocity at B by $\alpha_{ue,B}<1$. For $\alpha_{ue,B}=1$, anode sheath "collapses" and only a flat sheath potential can accept the electron flux coming from plasma. For $\alpha_{ue,B}>1$, new sheath model is required. Moreover, the modification of electron velocity on Bohm criteria in Eq. (11) is only negligible for $\alpha_{ue,B}^2\ll 1$. For these reasons, it is important to check α_{ue} to examine the validity of assumptions. In the current case, $\alpha_{ue,B}\approx 0.2$ (see Fig. 2) justifies the consistency of sheath models.

F. Electron energy conservation

The local balance of total electron energy is between the gradient of total energy flux and energy production rate due to electric field, collisions, and wall reactions. The dimensionless total energy equation writes

$$\frac{\mathrm{d}\hat{q}_e}{\mathrm{d}\hat{z}}+\frac{\mathrm{d}\left[\left(\hat{K}_{eD}+\hat{h}_e\right)\hat{u}_e\right]}{\mathrm{d}\hat{z}}=\hat{n}\hat{u}_e\frac{\mathrm{d}\hat{\phi}}{\mathrm{d}\hat{z}}+\hat{E}_e\ , \tag{28}$$

with $\hat{K}_{eD}=\hat{m}_e\hat{n}\hat{u}_e^2/2$ the directed kinetic energy and $\hat{h}_e=5\hat{n}\hat{T}_e/2$ the kinetic enthalpy. The electron mechanical energy balance is obtained by multiplying electron momentum equation with $\hat{u}_e$. After combining with continuity equation, it becomes

$$\hat{n}\hat{u}_e\frac{\mathrm{d}\hat{\phi}}{\mathrm{d}\hat{z}}-\frac{\mathrm{d}\left(\hat{K}_{eD}\hat{u}_e\right)}{\mathrm{d}\hat{z}}=\hat{u}_e\hat{R}_e-\frac{\hat{m}_e\hat{u}_e^2}{2}\hat{S}_e+\hat{u}_e\frac{\mathrm{d}\hat{p}_e}{\mathrm{d}\hat{z}}\ . \tag{29}$$

Inside plasma, electrons would gain kinetic energy if there is a positive electric work ($\hat{n}\hat{u}_e\,\mathrm{d}\hat{\phi}/\,\mathrm{d}\hat{z}$). In other words, as on the LHS of Eq. (29), the electric work is consumed to balance directed energy flux gradient

$\mathrm{d}\left(\hat{K}_{eD}\hat{u}_e\right)/\mathrm{d}\hat{z}$. The rest of electric work (on the RHS) will be transferred to change plasma internal energy. This "transfer" is mathematically shown by substituting Eq. (29) into Eq. (28), giving the internal energy equation as

$$\frac{\mathrm{d}\left(\hat{h}_e\hat{u}_e\right)}{\mathrm{d}\hat{z}} + \frac{\mathrm{d}\hat{q}_e}{\mathrm{d}\hat{z}} = \hat{E}_e + \hat{u}_e\hat{R}_e - \frac{\hat{n}_e\hat{u}_e^2}{2}\hat{S}_e + \hat{u}_e\frac{\mathrm{d}\hat{p}_e}{\mathrm{d}\hat{z}} \ . \tag{30}$$

The three "transferring" terms appear on the RHS, being frictional dissipation, consumption to sustain particle flux gradient, and pressure push work. From the results, taking into account dominant collisions, the internal energy balance can be approximated by

$$\frac{\mathrm{d}\left(\hat{h}_e\hat{u}_e\right)}{\mathrm{d}\hat{z}} + \frac{\mathrm{d}\hat{q}_e}{\mathrm{d}\hat{z}} \approx \hat{E}_{e,sw} + \hat{E}_{e,pw} + \hat{E}_{e,io} + \hat{n}\hat{u}_e\frac{\mathrm{d}\hat{\phi}}{\mathrm{d}\hat{z}} \ . \tag{31}$$

The contribution of each term in Eq. (31) is shown by the EE panel of Fig. 3. The main heating source to plasma is from thermionic electrons (*sw*). After being accelerated by strong electric field inside the insert sheath, they enter plasma at the sheath edge W, where they are considered immediately thermalized with plasma electrons. Escaped plasma electrons carry energy out with them (*pw*), yet small in this case because of sufficient sheath drop to repel them back. The net consequence of the insert sheath on electron energy is thus to convert electric work to electron kinetic energy that serves as energy source to the plasma. Electric work inside plasma (ϕ) tends to heat up plasma near the inlet and cool it down downstream. Energy is mostly spent in ionization (*io*) and changing fluxes of heat and enthalpy (q and h). With negligible temperature gradient, the enthalpy flux gradient would vary in an opposite manner to ionization spent as (see Fig. 3)

$$\frac{\mathrm{d}\left(\hat{h}_e\hat{u}_e\right)}{\mathrm{d}\hat{z}} \approx \frac{5}{2}\hat{T}_e\frac{\mathrm{d}\left(\hat{n}\hat{u}_e\right)}{\mathrm{d}\hat{z}} = \frac{5}{2}\hat{T}_e\hat{S}_e \ . \tag{32}$$

Heat flux gradient is thus adjusted accordingly to fulfil the local balance.

The *global* energy balance is obtained by the volumetric integration of Eq. (31) as

$$\hat{Q}_{eh,IB} + \hat{Q}_{eq,IB} \approx \hat{Q}_{e,sw} + \hat{Q}_{e,pw} + \hat{Q}_{e,io} + \hat{Q}_{e,\phi} \ . \tag{33}$$

The global energy production rate inside plasma is thus balanced with the energy fluxes that leave both ends. At the edges, they are considered to be carried by the high-energy tail of Maxwellian electrons, which must be consistent with the sheath drop that also agrees with the current balance. Using Eq. (9), the sheath thus regulates the energy flux by

$$\begin{aligned}\hat{Q}_{eh,IB} + \hat{Q}_{eq,IB} &\approx \hat{Q}_{e,IB} \\ &= \hat{I}_{e,B}\left(\hat{\phi}_{AB} + 2\hat{T}_{e,B}\right) - \hat{I}_{e,I}\left(\hat{\phi}_{JI} + 2\hat{T}_{e,I}\right) \ ,\end{aligned} \tag{34}$$

where the directed energy flux is considered negligible. This physical energy balance between plasma and sheath is translated, mathematically, to be the constraint $f_q = 0$.

IV. Parametric study

A. Discharge potential

Parametric study is first carried out by changing $\hat{\phi}_I$ (equivalent to change discharge potential $\hat{\phi}_A$). For comparison, the spatial profiles for $\hat{\phi}_I = 4, 5, 7$ and $T_s = 1650\,\mathrm{K}$ are displayed together in Fig. 2. Some other interesting properties are plotted against $\hat{\phi}_I$ (parametric plots) and shown by the solid curves in Fig. 4. The *global* conservations of particle, momentum, and energy are presented in Fig. 5.

First of all, as shown in Fig. 4 by the solid curve, $\hat{\phi}_A$ increases with $\hat{\phi}_I$ monotonically within the range of parameters chosen in this article. Based on this observation, the authors claim that multiple solutions did

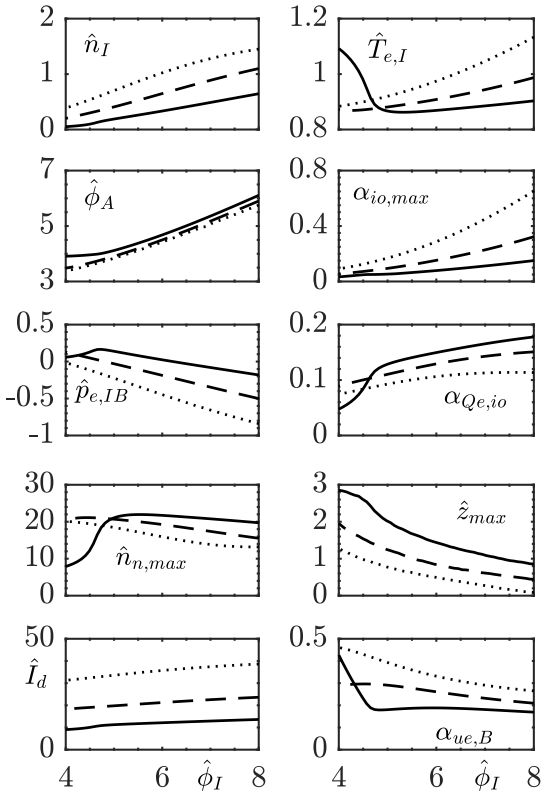

Figure 4: Parametric plots of $\hat{\phi}_I$ for different insert temperature: $T_s = 1650$K (solid), $T_s = 1700$K (dashed), $T_s = 1750$K (dotted). The $\alpha_{Qe,io}$ panel presents the ratio $\hat{Q}_{e,io}/\hat{Q}_{e,ews}$. The $\hat{z}_{max}$ panel shows the location of maximum neutral density.

not yet occur and an unique solution has been observed for the original implicit equations $\boldsymbol{f}(\hat{T}_{e,I}, \hat{n}_I, \hat{\phi}_I) = 0$. For this reason, parametric plots are still presented with $\hat{\phi}_I$ as the abscissa axis, treating $\hat{\phi}_I$ as a parameter for the problem $\boldsymbol{f}(\hat{T}_{e,I}, \hat{n}_I) = 0$.

By increasing discharge voltage, more power is available and more ionization can be expected. As shown by the α_{io} profiles in Fig. 2, the solid curve for $\hat{\phi}_I = 7$ has the highest ionization degree. Likewise, among the parametric plots in Fig. 4, both maximum ionization degree $\alpha_{io,max}$ and inlet plasma density $\hat{n}_I$ further confirm that ionization increases with discharge voltage. However, electron temperature $\hat{T}_{e,I}$ is found to increase for $\hat{\phi}_I \lessapprox 5$ and decrease for $\hat{\phi}_I \gtrapprox 5$. For this reason, two operational regimes are identified, named by LIO (Low IOnization) and HIO (High IOnization) regimes. Before exploring the origins and consequences of two regimes, global conservations are discussed first.

1. Global conservations

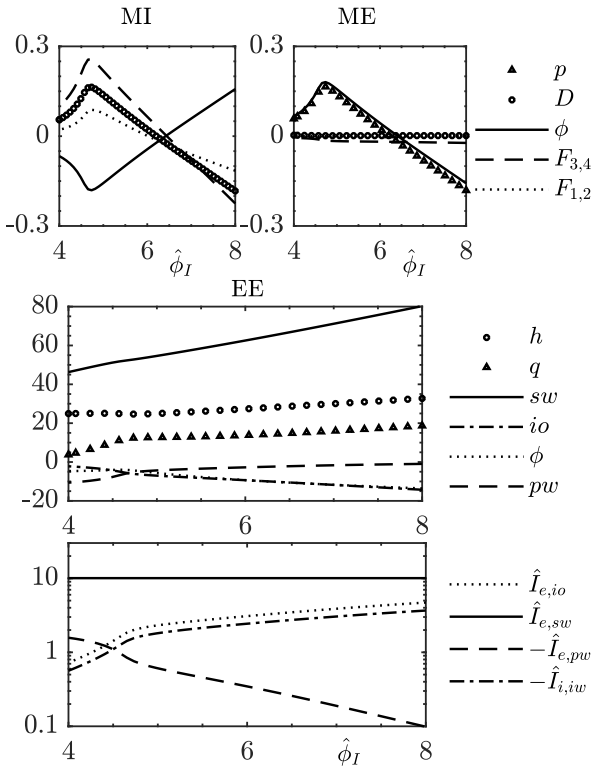

Figure 5: Global conservation of current, momentum, and energy for $T_s = 1650\,\mathrm{K}$. Same legends are used as those for local balances in Fig. 3.

The discharge current, as shown by Fig. 5 and Eq. (25), is composed by thermionic electron source ($\hat{I}_{e,sw} > 0$), plasma electron wall loss ($\hat{I}_{e,pw} < 0$), and plasma ion wall loss (yet as electron current source $-\hat{I}_{i,iw} > 0$). For the same cathode length and insert temperature, thermionic electron current $\hat{I}_{e,sw}$ does not change, being independent on discharge voltage. For plasma electrons, increased discharge voltage results in a higher insert sheath drop (ϕ_W), which reflects more electrons back to plasma thus reduces electron loss. For plasma ions, as shown by the curves of $-\hat{I}_{i,iw}$ and $\hat{I}_{i,io}$, increased ionization also results in more ion wall loss. After all, discharge current increases with discharge voltage (see $\hat{I}_d$ panel in Fig. 4) as a result of less plasma electrons and more plasma ions escaping from the plasma to the insert. Nevertheless, the discharge current does not increase much because it is dominated by the constant thermionic current.

For the global electron momentum conservation in Fig. 5, electron inertia (directed momentum flux) is negligible as found before. Thus the volumetric integration of electric force $\hat{M}_{e,\phi} = \int_0^{\hat{z}_B} \hat{n}\,\mathrm{d}\hat{\phi}$ roughly balances with the pressure difference $\hat{p}_{e,IB}$. Nevertheless, globally, collisional forces are not that marginal as for the local balance in Fig. 3. This is because that, with $\hat{u}_e > 0$ nearly everywhere, electric field accelerates and de-accelerates electrons at different regions (see $\hat{\phi}$ profiles in Fig. 2). On the other hand, with $\hat{u}_e > \hat{u}_{i,n}$ nearly everywhere, collisions on electrons mainly serve as friction. Consequently, with some influence of electric field being cancelled out by volumetric integration, the contribution of collisions in the global conservation is more pronounced.

For the plasma momentum balance, as proved in Sec. D, sonic conditions at both ends result in $\hat{M}_{iD,IB} + \hat{M}_{eD,IB} = \hat{M}_{ep,IB} = \hat{p}_{e,IB}$. This can now be clearly observed from the MI and ME panels in Fig. 5. Also, according to Eq. (27), the electron pressure difference ($\hat{M}_{ep,IB} = \hat{p}_{e,IB}$) is balanced with collisions that govern ion response ($2\hat{M}_{ep,IB} \approx \hat{M}_{i,R}$). If collisions globally introduce more backward momentum on ions, electric field is found to direct ions and electrons forward and backward, respectively. Then, due to electron pressure gradient roughly balanced with electric force, the electron pressure at B becomes smaller than that at I. Here, another feature that distinguishes two regimes can be noticed. In the HIO regime, for increasing discharge voltage, the net effect of electric and collisional forces tends to direct ion momentum more backward (or less forward), together with a decreasing electron pressure difference $\hat{p}_{e,IB}$.

For the global energy conservation in Eq. (33), the contribution of each term is shown in the EE panel of Fig. 5. As discussed in Sec. F, the main energy source for the plasma is the kinetic energy of thermionic electrons ($\hat{Q}_{e,sw}$) that are accelerated by electric field inside the sheath. Since the insert sheath drop $\hat{\phi}_W$ increases with $\hat{\phi}$ and thus discharge voltage, more electric power is transferred to plasma due to increased $\hat{Q}_{e,sw}$. Around half of this energy source leaves plasma at both ends as enthalpy and heat fluxes ($\hat{Q}_{eh,IB}$ and $\hat{Q}_{eq,IB}$, respectively). The rest is spent mainly in ionization ($\hat{Q}_{e,io}$), electric work ($\hat{Q}_{e,\phi}$), and balancing plasma electron loss at W ($\hat{Q}_{e,pw}$).

The axial electric work inside plasma is found to be negative ($\hat{Q}_{e,\phi} < 0$) in Fig. 5. That is to say, inside plasma, internal electron energy is converted to electrical energy. This needs to be explained from the local balance Eq. (31). Negative electric work $\hat{I}_e\,\mathrm{d}\hat{\phi}/\,\mathrm{d}\hat{z} < 0$ mainly occurs at the electron-repelling region downstream with $\hat{I}_e > 0$ and $\mathrm{d}\hat{\phi}/\,\mathrm{d}\hat{z} < 0$ (see Fig. 3). In this region, $\hat{I}_e$ can be much larger than that of upstream where electric field is electron-accelerating with $\hat{I}_e > 0$ and $\mathrm{d}\hat{\phi}/\,\mathrm{d}\hat{z} > 0$. For this reason, negative electric work thus occurs in the global energy conservation, as being dominated by the downstream electron-repelling region. It is important to note that this negative electric work is a result of separating insert-wall sheath (that accelerates thermionic electrons) and quasi-neutral plasma. Considering both together as the ionized gas inside cathode, the net electric work on electrons must be positive for being the only energy source.

The energy spent on ionization ($\hat{Q}_{e,io}$) is found to increase with discharge voltage, the same as its ratio to the thermionic electron energy source (see $\alpha_{Q_{e,io}} = \hat{Q}_{e,io}/\hat{Q}_{e,ews}$ in Fig. 4). In the LIO regime, for a decreasing discharge voltage drop, it can be seen that $\alpha_{Q_{e,io}}$ drops much faster than that in the HIO regime. Cathode thus spends much less energy on ionization in the LIO regime. It even drops to be less than the energy taken away by the plasma electrons at the insert sheath edge W, i.e., $|\hat{Q}_{e,pw}| > |\hat{Q}_{e,io}|$. This is consistent with the fact that, for a smaller sheath drop ϕ_W, there are more plasma electrons escaping to the insert. Interestingly, for the same reason, ions would arrive at the insert surface with less energy due to reduced acceleration by sheath. Although insert thermal balance is beyond the scope of this article, the authors carried out rough calculations to compare the energy fluxes of plasma electrons and ions at insert surface S. It was found that, in the LIO regime, plasma electron bombardment is the main insert heating mechanism. Ion bombardment dominates in the HIO regime. However, thorough study on insert thermal balance will be left for future work.

2. LIO and HIO regimes

The main characteristics that distinguish the LIO regime from the HIO regime have been found: electron temperature *drops* with discharge voltage (see Fig. 4); more discharge voltage results in ion momentum to be more forward-directed (see Fig. 5), together with an increasing electron pressure difference $\hat{p}_{e,IB}$.

To understand the differences of two regimes, it is necessary to go back to the implicit equations $\boldsymbol{f}(\hat{T}_{e,I}, \hat{n}_I) = 0$. How these two unknowns are found to satisfy $\boldsymbol{f}(\boldsymbol{x}) = 0$ resembles how plasma adjusts itself to fulfil sonic conditions and global energy conservation. Although electron temperature can not be determined without energy equation, energy conservation can not explain the non-monotonic $\hat{T}_{e,I}$ behaviour on $\hat{\phi}_I$. It is found out to be a result of the first constraint. That is to say, to increase ion velocity from $\hat{u}_{i,I} \approx -1$ at I to $\hat{u}_{i,I} \approx 1$ at B,[a] $\hat{n}_I$ and $\hat{T}_{e,I}$ need to reach an agreement. For this reason, the authors have studied how $f_z = z_B - z_B^*$ changes with $\boldsymbol{x} = [\hat{T}_{e,I}; \hat{n}_I]$.

Mathematically speaking, for a fixed $\hat{T}_{e,I}$, f_z was found to decrease with $\hat{n}_I$ in the LIO regime, yet increase in the HIO regime.[b] On the other hand, f_z was found to decrease with $\hat{T}_{e,I}$ monotonically. It seems like that, in the LIO regime, increasing $\hat{n}_I$ (with constant $\hat{T}_{e,I}$) would result in ions to be too fast downstream and the sonic condition is thus achieved before B. To counteract this effect, $\hat{T}_{e,I}$ needs to be reduced so that ions are slowed down and the sonic condition is achieved at B. The opposite occurs in the HIO regime. Guided by these mathematical behaviours of $f_z(\hat{T}_{e,I}, \hat{n}_I)$, we can then come back to the spatial profiles and parametric plots to discuss the physical implications underneath.

As discussed in Sec. E, ionization frequency $\hat{\nu}_{io}$ was found to play an important role in determining ion velocity gradient. It can be the value of $\hat{\nu}_{io}$ that is adjusted by $\hat{T}_{e,I}$ and $\hat{n}_I$ to have adequate ion velocity gradient, thus achieving sonic conditions. The LIO regime is analysed by comparing the dotted ($\hat{\phi}_I = 4$) and the dashed ($\hat{\phi}_I = 5$) profiles in Fig. 2. Since higher discharge voltage results in higher plasma density $\hat{n}_I$, neutral density at inlet also increases (see Fig. 2) due to $\hat{u}_{i,I} \approx -1$ and $\hat{n}_{n,I} = (1 - \hat{n}_I \hat{u}_{i,I})/\hat{u}_{n,I}$. Therefore, a higher ionization frequency $\hat{\nu}_{io}$ could be expected. Surprisingly, in the $\hat{F}_2$ profiles, the $\hat{\phi}_I = 5$ curve lies below the $\hat{\phi}_I = 4$ curve near the inlet. Because of $\hat{\nu}_{iw} = 1$ in our simulations, it can only be a lower electron temperature $\hat{T}_{e,I}$ that reduces $\hat{\nu}_{io}$ (and thus $\hat{F}_2 = \hat{\nu}_{io} - \hat{\nu}_{iw}$). Following the trend of $\hat{\nu}_{io}$, ion velocity gradient (see $\hat{u}_i$ in Fig. 2) for the $\hat{\phi}_I = 5$ case is smaller upstream and ions are "slower" (with a more negative velocity). Around the mid-point, the effect of increased neutral density finally takes over to increase $\hat{\nu}_{io}$, which leads to faster ions downstream for $\hat{\phi}_I = 5$. At the end, with increasing discharge voltage and higher plasma density in the LIO regime, if electron temperature was not reduced to achieve a lower $\hat{\nu}_{io}$, ions would be too fast to achieve the sonic condition at B.

The specific solution presented in Sec. III for $\hat{\phi}_I = 7$ belongs to the HIO regime. Compared to the profiles for $\hat{\phi}_I = 5$, a higher $\hat{\nu}_{io}$ (also $\hat{F}_2$) is observed in the region next to the inlet, being consistent with higher $\hat{n}_I$ and $\hat{n}_{n,I}$. Then, ion velocity increases with $\hat{z}$ much faster and maximum neutral density occurs much closer to the inlet (see $\hat{u}_i$ and $\hat{n}_n$ profiles in Fig. 2). After this maximum, ionization consumes neutrals and $\hat{\nu}_{io}$ drops abruptly (see Sec. B). It then occurs the region with $\hat{\nu}_{io} < \hat{\nu}_{iw}$ and $\hat{F}_2 < 0$, where ionization becomes less than wall loss. As discussed in Sec. E, this effect suppresses ion velocity gradient. It is the existence of such a region with $\hat{F}_2 < 0$ that identifies the HIO regime. As shown by the $\hat{z}_{max}$ plot in Fig. 4, in the HIO regime, the location of maximum neutral density drops with $\hat{\phi}_I$. Therefore, ions travel a longer distance with $\hat{F}_2 < 0$ that reduces $\mathrm{d}\hat{u}_i/\,\mathrm{d}\hat{z}$. To counteract this effect and to have sufficient ion speed to reach sonic condition at B, a higher electron temperature is thus required to increase $\hat{\nu}_{io}$.

In conclusion, in the LIO regime, because ionization is not yet sufficient for the region with $\hat{F}_2 < 0$ to occur, more discharge voltage leads to higher plasma density, which tends to increase ion velocity and a reduction in electron temperature is thus necessary to slow down ions and have sonic condition at B. In the HIO regime, ionization is so high that a region with $\hat{F}_2 < 0$ occurs downstream. If discharge voltage is increased, ions travel a longer distance with a suppressed velocity gradient and an increase in electron

[a] For the purpose of this discussion, the influence of electron temperature and electron velocity on ion sonic velocities in Eqs. (7) and (11) can be ignored due to $\sqrt{\hat{T}_e} \approx 1$ and $\alpha_{ue,B} \ll 1$.

[b] It is actually this non-monotonic behaviour that results in the existence of two solutions if energy equation is not solved (see Sec. III).

temperature is necessary to have fast enough ions and thus reach sonic condition at B. Similarly, also due to such a region with $\hat{F}_2 < 0$ in the HIO regime, increasing $\hat{\phi}_I$ results in ions to travel a longer region with $\hat{u}_i > \hat{u}_n$. For this reason, globally, collisions introduce less forward momentum on ions as shown in Fig. 5. Eventually, it occurs the situation $\hat{p}_{e,B} < \hat{p}_{e,I}$ and ion momentum is globally directed backwards.

B. Insert temperature

The parametric plots on $\hat{\phi}_I$ are presented in Fig. 4 for three different insert temperature, $T_s = 1650\,\mathrm{K}$ ($\hat{T}_s \approx 0.0356$, $\hat{S}_{e,sw} \approx 3.352$, solid), $T_s = 1700\,\mathrm{K}$ ($\hat{T}_s \approx 0.0366$, $\hat{S}_{e,sw} \approx 6.170$, dashed), $T_s = 1750\,\mathrm{K}$ ($\hat{T}_s \approx 0.0377$, $\hat{S}_{e,sw} \approx 10.98$, dotted). Based on previous discussions, the influence of thermionic emission on plasma response can be discussed straightforwardly. Insert temperature can influence both flux of thermionic electrons ($\hat{S}_{e,sw}$) and average energy carried by one electron ($\hat{\varepsilon}_{sw}$). With the former increasing exponentially with $\hat{T}_s$ and the latter linearly, the influence of the latter is negligible. Since thermionic electron source is the dominant term in current balance, discharge current $\hat{I}_d$ increases with insert temperature $\hat{T}_s$. With thus increased electric power, more ionization can be expected as shown by higher $\hat{n}_I$ and $\alpha_{io,max}$. It is interesting to note that, although more energy is spent on ionization, the portion it takes ($\alpha_{Q_{e,io}}$) is less. Increased ionization causes the cathode to work more in the HIO regime. For this reason, maximum neutral density drops, its location occurs closer to the inlet, ion momentum is directed more backward by collisions, there is more negative pressure difference $\hat{p}_{e,IB}$, and electron temperature is thus permitted to increase with available electric power.

At the end, the authors would like to discuss about the electron velocity ratio $\alpha_{ue,B}$. As shown by Fig. 4, in the HIO regime, $\alpha_{ue,B}$ is increased with thermionic electron flux $\hat{S}_{e,sw}$. Fast electrons also occur in the LIO regime of the solid curve with the lowest $\hat{S}_{e,sw}$. As that discussed for ion velocity gradient, electron velocity gradient is also closely related to particle production frequencies $\hat{F}_1 = \hat{\nu}_{sw} + \hat{\nu}_{io} - \hat{\nu}_{pw}$. Since thermionic emission is the dominant effect, high thermionic electron source $\hat{S}_{e,sw}$ and low plasma density $\hat{n}$ can both result in fast electrons, by increasing thermionic emission frequency as $\hat{\nu}_{sw} = \hat{S}_{e,sw}/\hat{n}$. Therefore, the assumption of an electron-repelling anode sheath (requiring $\alpha_{ue,B} \ll 1$) would break down for sufficiently low discharge voltage. For this reason, simulations were not carried out for $\hat{\phi}_I < 4$ in this work. Nevertheless, there are two more problems for lower discharge voltages. At first, in some cases of the LIO regime where solution exists for $\boldsymbol{f}(\boldsymbol{x}) = 0$, numerical difficulties were encountered. For further smaller discharge voltage, there exists no solutions and the authors suspect a regular sonic transition inside the quasi-neutral plasma. These effects will be explored in future works.

V. Discussions and conclusions

A quasi-neutral, steady-state, 1D axial fluid model for the hollow cathode insert region has been presented in this work. As a consequence of variable separation and decoupling, wall reactions appear together with collisions as source or sink terms. Two operational regimes are identified, named LIO and HIO regimes. For one set of plasma parameters in the HIO regime, the spatial profiles of plasma variables are used to discuss the plasma response, together with the local and global balances of particle, momentum, and energy.

Owing to small electron mass and thus high thermal conductivity, the electron temperature is almost constant along $\hat{z}$. Due to negligible electron inertia in the local electron momentum balance, electric field is locally balanced with pressure gradient. Ion inertia is found to be not negligible. Nevertheless, combining ion momentum and continuity equations, electric field is locally balanced with collisions that govern ion response ($\hat{F}_4$, except near the singularities at the boundaries), as shown in Eq. (21). The maxima of density and potential thus occur near $\hat{u}_i \approx \hat{u}_n$. For neutrals, as a result of negligible neutral pressure ($\hat{T}_n \approx 0$) and sufficient CEX exchange collisions, maximum neutral density occurs near $\hat{\nu}_{io} \approx \hat{\nu}_{iw}(1 - \hat{u}_i/\hat{u}_n)$. Before this maximum, neutral density increases because they are slowed down by collisions. After this maximum, it decreases because ionization consumes neutrals. In the HIO regime, for the reason of strong ionization, neutral density drops greatly, which reduces ionization frequency and ionization no longer compensates wall loss. The occurrence of such a region downstream with $\hat{F}_2 = \hat{\nu}_{io} - \hat{\nu}_{iw} < 0$ identifies the HIO regime.

For global conservations of particle and momentum, the volumetric integration of the source and sink terms is balanced with the fluxes that leave the quasi-neutral plasma at the sheath edges. Due to floating condition at the back plate, the discharge current arriving at the anode is balanced with the current at the insert wall. Thermionic electron emission and ion recombination are sources of discharge current, with plasma electron loss as a sink of current. Since sonic conditions are applied at both ends, the electron pressure difference is related to collisional momentum production rates on ions by $2(\hat{p}_{e,B} - \hat{p}_{e,I}) \approx \int_o^{\hat{z}_B} \hat{R}_i \, \mathrm{d}\hat{z}$. If ion momentum is globally directed backward, the pressure at B drops below that at I.

For electron energy balance, the main energy source is the kinetic energy of thermionic electrons at W, which originates from their electric potential energy inside the sheath. Inside the quasi-neutral plasma, electric work is indirectly transferred to electric internal energy mainly through pressure push work. Nevertheless, the global electric work inside plasma is found to be negative, which occurs owing to the artificial separation of sheath and plasma regions. The rest of the energy source, after mainly being spent in ionization, leaves plasma at the boundaries.

After understanding the spatial profiles, parametric studies were carried out by varying discharge voltage. By increasing discharge voltage, more electric power results in higher plasma density and ionization degree. Because discharge current is still dominated by thermionic emission at a constant temperature, discharge current increases slightly for more ions and less plasma electrons arriving at the insert wall.

The two operational regimes can be easily distinguished from the parametric plots. Electron temperature drops with discharge voltage in the LIO regime and increases in the HIO regime. The reason for this lies in the sonic conditions applied for a fixed cathode length (the constraint $f_z = 0$), which is related to ion velocity gradient and particle production frequency $\hat{F}_2 = \hat{\nu}_{io} - \hat{\nu}_{iw}$. In the LIO regime, to counteract the effect of increased plasma density that rises $\hat{\nu}_{io}$ and thus leads to faster ions, electron temperature is thus reduced to bring down $\hat{\nu}_{io}$ and slow down ions, thus satisfying sonic condition at B. In the HIO regime, ionization is so high that a region with $\hat{F}_2 < 0$ occurs downstream, in which ion velocity gradient is suppressed. If discharge voltage is increased, more plasma density elongates such a region. To speed up ions and achieve sonic condition at B, an increase in electron temperature is necessary to have sufficient $\hat{\nu}_{io}$. For the same reason, in the HIO regime, ions travel in a longer distance with $\hat{u}_i > \hat{u}_n$, in which collisions introduce backward momentum on ions. The pressure difference $\hat{p}_{e,IB}$ thus drops with $\hat{\phi}_I$.

The existence of LIO and HIO regimes is also a manifestation of the non-monotonic behaviour of $f_z = z_B - z_B^*$ on $\hat{n}_{z,I}$. In the LIO regime, f_z reduces with $\hat{n}_{z,I}$, otherwise in the HIO regime. For this reason, if electron energy conservation is not taken into account, two solutions are normally found for $f_z = 0$, yet with one of them far-away from being consistent with energy conservation. Consequently, it is necessary to include energy equation. However, as shown by the discussion above for two regimes, electron temperature is not only determined by the energy equation. It must agree with $\hat{n}_I$ to have adequate ion velocity gradient and thus satisfy sonic conditions at the boundaries. The difficulties in discussing the causality of plasma responses can also be revealed at this point.

Parametric plots were compared for different insert temperature. By increasing insert temperature, discharge current increases with the flux of thermionic electrons at insert wall. For the same discharge voltage, electric power is thus increased. Therefore, there are more ionization and cathode works more in the HIO regime.

Acknowledgement

This work was supported by the Ministerio de Economía y Competitividad of Spain (Grants FJCI-2016-28742 and ESP-2016-75887).

A. Wall reactions

Thermionic electrons emitted by the insert is a source of electrons and the associated particle production rate follows Richardson-Dushman law as

$$S_{e,sw} = n\nu_{sw} = n\frac{2}{R}\frac{A_G}{e}T_{sK}^2 \exp\left(-\frac{\phi_{wf}}{T_{sV}}\right) \ , \tag{35}$$

with ϕ_{wf} the insert work function in eV, T_{sV} the insert temperature in eV (T_{sK} in K), and A_G the material-dependent generalized Richardson constant in $\mathrm{A\,m^{-2}\,K^{-2}}$. Compared to the particle flux, the factor $2/R$ appears as a result of cross-sectional average. This flux can be increased by Schottky effect, or decreased by space-charge-limited effect. However, these effects are not considered in this work. Moreover, without a thermal model for the insert and cathode tube, the temperature of the insert T_s is considered constant. Before taking into account a variable flux, it is beneficial to first understand the influence of thermionic emission on the simulation results as being constant everywhere. One thermionic electron is emitted at insert with zero axial velocity in the directed motion, yet with random energy as the insert temperature T_s. Because a radial electric field accelerates electrons in the sheath, these electrons do not contribute to momentum equation due to zero axial velocity. However, in average, one electron gains more kinetic energy from sheath potential drop as $e\phi_W$. Consequently, as source of energy, the energy density production rate from thermionic emission reads

$$E_{e,sw} = n\nu_{sw}\varepsilon_{sw}, \quad \varepsilon_{sw} \approx e\phi_W + T_s \ . \tag{36}$$

The sheath potential drop is given by $\phi_W = \phi + \phi_R$, with ϕ_R being the change of potential from the centreline to the edge $r = R$.

With negligible electron directed motion compared to random thermal motion, plasma electrons are near-Maxwellian at W. Considering a conventional electron-repelling sheath, only electrons with energy larger than ϕ_W can escape plasma. As a sink of particles, the associated particle density production rate is given by

$$S_{e,pw} = -n\nu_{e,pw}, \tag{37}$$

$$\nu_{e,pw} = \frac{2}{R}n_R\sqrt{\frac{T_eT_{eR}}{2\pi m_e}} \exp\left[-\frac{e\phi_W}{T_eT_{eR}}\right] \ , \tag{38}$$

where n_R and T_{eR} denote the ratio between the value at R and the cross-sectional average. Escaped plasma electrons take away momentum with them and manifest as a sink of momentum. The momentum production rate writes

$$R_{e,pw} = -m_e n\nu_{pw}u_e \ . \tag{39}$$

These high-energy electrons carry energies away with them, giving the energy production rate as

$$E_{e,pw} = -n\nu_{pw}\varepsilon_{pw}, \quad \varepsilon_{pw} = e\phi_W + 2T_eT_{eR} \ . \tag{40}$$

Ions arrive at W with Bohm velocity, which gives the particle and momentum production rates as

$$S_{i,iw} = -n\nu_{iw}, \quad R_{i,iw} = -n\nu_{iw}u_i, \tag{41}$$

$$\nu_{iw} = \frac{2}{R}n_R\sqrt{\frac{T_eT_{eR}}{m_i}} \ . \tag{42}$$

After bombarding on the wall, ions return to plasma as neutrals with the same amount of particle flux, thus $S_{n,iw} = -S_{i,iw} > 0$ as source of neutrals. Considering 100% accommodation, neutrals come back with zero axial velocity, thus $R_{n,iw} = 0$.

Above wall reaction frequencies can be evaluated after that the three R-related properties (n_R, T_{eR}, ϕ_R) are calculated by solving radial equations. In this work, without including the radial model, approximate relations are used as

$$n_R = 0.5, \quad e\phi_R/T_e = \ln(n_R) \approx -0.69, \quad T_{eR} = 1 \ , \tag{43}$$

with constant temperature along r, plasma density at $r = R$ as half of the cross-sectional average, and plasma potential decay approximated by Boltzmann relation.

B. Dimensionless collisional terms

The particle production terms $\hat{F}_{1,2}$ are

$$\hat{F}_1 = \hat{\nu}_{io} + \hat{\nu}_{sw} - \hat{\nu}_{pw}, \quad \hat{F}_2 = \hat{\nu}_{io} - \hat{\nu}_{iw} \ , \tag{44}$$
$$\hat{\nu}_{io} = \nu_{io}/\nu_0, \quad \hat{\nu}_{sw} = S_{e,sw}/(\hat{n}S_0), \quad \hat{\nu}_{iw} = \sqrt{\hat{T}_e} \ ,$$
$$\hat{\nu}_{pw} = \sqrt{\frac{\hat{T}_e}{2\pi\hat{m}_e}} \exp\left(-\frac{\hat{\phi}_W}{\hat{T}_e}\right) \ .$$

The combination of continuity and momentum equations lead to $\hat{F}_{3,4,5}$, which are

$$\hat{F}_3 = -\hat{\nu}_{ei}\left(\hat{u}_e - \hat{u}_i\right) - \hat{\nu}_{en}\left(\hat{u}_e - \hat{u}_n\right)$$
$$- \hat{m}_e\left(\hat{\nu}_{io} + \hat{\nu}_{e,sw}\right)\hat{u}_e \ , \tag{45}$$
$$\hat{F}_4 = \hat{\nu}_{ei}(\hat{u}_e - \hat{u}_i) - \left(\hat{\nu}_{io} + \hat{\nu}_{in}\right)\left(\hat{u}_i - \hat{u}_n\right) \ , \tag{46}$$
$$\hat{F}_5 = \frac{\hat{n}}{\hat{n}_n}\left[\hat{\nu}_{en}(\hat{u}_e - \hat{u}_n) + \hat{\nu}_{in}\left(\hat{u}_i - \hat{u}_n\right) - \hat{\nu}_{iw}\hat{u}_n\right] \ , \tag{47}$$
$$\hat{\nu}_{en} = \hat{m}_e\nu_{en}/\nu_0, \ \hat{\nu}_{ei} = \hat{m}_e\nu_{ei}/\nu_0 \ , \ \hat{\nu}_{in} = \nu_{in}/(2\nu_0) \ .$$

The energy-related term $\hat{F}_6$ writes

$$\hat{F}_6 = \hat{E}_e + \hat{E}_{eR} + \hat{E}_{eS} \ , \tag{48}$$

with the energy production rates in $\hat{E}_e$ given by

$$\hat{E}_{e,sw} = \hat{n}\hat{\nu}_{se}\hat{\varepsilon}_{sw}, \qquad \hat{\varepsilon}_{sw} = \hat{\phi}_W + \hat{T}_s \ ,$$
$$\hat{E}_{e,pw} = -\hat{n}\hat{\nu}_{pw}\hat{\varepsilon}_{pw}, \qquad \hat{\varepsilon}_{pw} = 2\hat{T}_e + \hat{\phi}_W \ ,$$
$$\hat{E}_{e,ei} = -3\hat{n}\hat{T}_e\hat{\nu}_{ei}, \qquad \hat{E}_{e,en} = -3\hat{n}\hat{T}_e\hat{\nu}_{en} \ ,$$
$$\hat{E}_{e,io} = -\hat{n}\hat{\nu}_{io}\hat{\varepsilon}_{io} \ ,$$

the friction dissipation term being

$$\hat{E}_{eR} \approx \hat{n}\left(\hat{\nu}_{en} + \hat{\nu}_{ei} + \hat{m}_e\hat{\nu}_{pw}\right)\hat{u}_e^2 \ ,$$

and the term from continuity equation as

$$\hat{E}_{eS} = \left(\frac{\hat{m}_e\hat{u}_e^2}{2} - \frac{5}{2}\hat{T}_e\right)\hat{n}\hat{F}_1 \ .$$

The temperature gradient term is

$$\hat{F}_7 = -\frac{\hat{q}_e}{\hat{\mathcal{K}}_e} \ , \quad \hat{\mathcal{K}}_e = \frac{5}{2}\frac{\hat{n}\hat{T}_e}{\hat{\nu}_{ei} + \hat{\nu}_{en}} \ . \tag{49}$$

References

[1] H. Kaufman, "Technology of electron-bombardment ion thrusters," *Advances in Electronics and Electron Physics*, vol. 36, no. C, pp. 265–373, 1975.

[2]D. M. Goebel, K. K. Jameson, R. M. Watkins, I. Katz, and I. G. Mikellides, "Hollow cathode theory and experiment. I. plasma characterization using fast miniature scanning probes," *J. Appl. Phys.*, vol. 98, no. 11, p. 113302, 2005.

[3]D. Warner, R. Branam, W. Hargus Jr., and D. Goebel, "Low current cerium hexaboride and lanthanum hexaboride hollow cathodes," in *Proceedings of 46th AIAA Aerospace Sciences Meeting and Exhibit*. Reno, NV, United States: AIAA, 2008, pp. 2008–1086.

[4]D. Lev, I. Mikellides, D. Pedrini, A. Benjamin, and M. McDonald, "Recent progress in research and development of hollow cathodes for electric propulsion," *Rev. Mod. Plasma Phys.*, vol. 3, no. 6, 2019.

[5]J. Sanmartin, M. Martinez-Sanchez, and E. Ahedo, "Bare wire anodes for electrodynamic tethers," *J. Propul. Power*, vol. 9, no. 3, pp. 353–359, 1993.

[6]R. Olsen, "Modification of spacecraft potentials by plasma emission," *J . Spacecr. Rockets*, vol. 18, no. 5, pp. 462–469, 1981.

[7]W. Deininger, G. Aston, and L. Pless, "Hollow cathode plasma source for active spacecraft charge control," *Rev. Sci. Instrum.*, vol. 58, no. 6, pp. 1053–1062, 1987.

[8]D. Siegfried, "A phenomenological model for orificed hollow cathodes," Ph.D. dissertation, Colorado State Univ., 1982.

[9]D. Pedrini, R. Albertoni, F. Paganucci, and M. Andrenucci, "Theoretical model of a lanthanum hexaboride hollow cathode," *IEEE Trans. Plasma Sci.*, vol. 43, no. 1, pp. 209–217, 2015.

[10]J. Mizrahi, V. Vekselman, V. Gurovich, and Y. Krasik, "Simulation of plasma parameters during hollow cathodes operation," *J. Propul. Power*, vol. 28, no. 5, pp. 1134–1137, 2012.

[11]D. Pedrini, T. Misuri, F. Paganucci, and M. Andrenucci, "Development of hollow cathodes for space electric propulsion at Sitael," *Aerospace*, vol. 4, no. 2, p. 26, 2017.

[12]C. Wordingham, P. Taunay, and E. Choueiri, "A critical review of orificed hollow cathode modeling," in *Proceedings of 53rd AIAA/SAE/ASEE Joint Propulsion Conference*. Atlanta, GA, United States: AIAA, 2017, p. 4888.

[13]I. Mikellides, I. Katz, D. M. Goebel, and J. Polk, "Hollow cathode theory and experiment. II. A two-dimensional theoretical model of the emitter region," *J. Appl. Phys.*, vol. 98, no. 11, p. 113303, 2005.

[14]G. Sary, L. Garrigues, and J. Boeuf, "Hollow cathode modeling: I. A coupled plasma thermal two-dimensional model," *Plasma Sources Sci. Technol.*, vol. 26, no. 5, p. 055007, 2017.

[15]I. Mikellides and I. Katz, "Wear mechanisms in electron sources for ion propulsion, 1: Neutralizer hollow cathode," *J. Propul. Power*, vol. 24, no. 4, pp. 855–865, 2008.

[16]I. Mikellides, I. Katz, D. Goebel, K. Jameson, and J. Polk, "Wear mechanisms in electron sources for ion propulsion, 2: Discharge hollow cathode," *J. Propul. Power*, vol. 24, no. 4, pp. 866–879, 2008.

[17]I. Mikellides, "Effects of viscosity in a partially ionized channel flow with thermionic emission," *Phys. Plasmas*, vol. 16, no. 1, p. 013501, 2009.

[18]B. Jorns, C. Dodson, D. Goebel, and R. Wirz, "Propagation of ion acoustic wave energy in the plume of a high-current LaB_6 hollow cathode," *Phys. Rev. E*, vol. 96, no. 2, p. 023208, 2017.

[19]A. Salhi, "Theoretical and experimental studies of orificed, hollow cathode operation," Ph.D. dissertation, Ohio State University, 1993.

[20]I. Katz, J. Anderson, J. Polk, and J. Brophy, "One-dimensional hollow cathode model," *J. Propul. Power*, vol. 19, no. 4, pp. 595–600, 2003.

[21]X. Chen, J. Navarro-Cavalle, and E. Ahedo, "Hollow cathode modelling: a macroscopic variable-separation approach," in *Proceedings of 6th International Conference on Tethers in Space*, Madrid, Spain, 2019.

[22]E. Ahedo, J. M. Gallardo, and M. Martinez-Sanchez, "Effects of the radial plasma-wall interaction on the Hall thruster discharge," *Phys. Plasmas*, vol. 10, no. 8, pp. 3397–3409, 2003.

[23]E. Ahedo and J. Navarro-Cavalle, "Helicon thruster plasma modeling: Two-dimensional fluid-dynamics and propulsive performances," *Phys. Plasmas*, vol. 20, no. 4, p. 043512, 2013.

[24]E. Ahedo, "Radial macroscopic model of a plasma flowing along annular dielectric walls," *Phys. Plasmas*, vol. 9, no. 7, pp. 3178–3186, 2002.

[25]V. Golant, A. Zhilinsky, and I. Sakharov, *Fundamentals of Plasma Physics*, ser. Wiley Series in Plasma Physics. John Wiley, 1980.

[26]D. M. Goebel, R. M. Watkins, and K. K. Jameson, "LaB6 hollow cathodes for ion and hall thrusters," *J. Propul. Power*, vol. 23, no. 3, pp. 552–558, 2007.